First fringes with an integrated-optics beam combiner at 10 μm. A new step towards instrument miniaturization for mid-infrared interferometry

L. Labadie, G. Martín, N. C. Anheier, B. Arezki, H. A. Qiao, B. Bernacki, P. Kern

A&A 531, A48 (2011)
DOI: 10.1051/0004-6361/201116727

Astronomy & Astrophysics

First fringes with an integrated-optics beam combiner at 10 μm

A new step towards instrument miniaturization for mid-infrared interferometry

L. Labadie[1,4,5], G. Martín[2], N. C. Anheier[3], B. Arezki[2], H. A. Qiao[3], B. Bernacki[3], and P. Kern[2]

[1] Instituto de Astrofisica de Canarias, C/ Via Lactea s/n, La Laguna, 38200 Tenerife, Spain
e-mail: labadie@iac.es
[2] UJF-Grenoble 1/CNRS-INSU, Institut de Planétologie et d'Astrophysique de Grenoble (IPAG) UMR 5274, 38041 Grenoble, France
[3] Pacific Northwest National Laboratory, 902 Battelle Boulevard, PO Box 999, Richland, 99352 Washington, USA
[4] Departamento de Astrofisica, Universidad de La Laguna, 38205 La Laguna, Tenerife, Islas Canarias, Spain
[5] I. Physikalisches Institut, Universität zu Köln, Zülpicher Str. 77, 50937 Köln, Germany

Received 15 February 2011 / Accepted 12 April 2011

ABSTRACT

Context. Observations of milliarcsecond-resolution scales and high dynamic range hold a central place in the exploration of distant planetary systems in order to achieve, for instance, the spectroscopic characterization of exo-Earths or the detailed mapping of their protoplanetary disc birthplace. Multi-aperture infrared interferometry, either from the ground or from space, is a very powerful technique to tackle these goals. However, significant technical efforts still need to be undertaken to achieve a simplification of these instruments if we wish to recombine the light from a large number of telescopes. Integrated-optics concepts appear to be a suitable alternative to the current conventional designs, especially if their use can be extended to a higher number of astronomical bands.
Aims. This article reports, for the first time to our knowledge, the experimental demonstration of the feasibility of an integrated-optics approach to mid-infrared beam combination for single-mode stellar interferometry.
Methods. We fabricated a two-telescope beam combiner prototype integrated on a substrate of chalcogenide glass, a material transparent from ~1 μm to ~14 μm. We developed laboratory tools to characterize in the mid-infrared the modal properties and the interferometric capabilities of our device.
Results. We obtain interferometric fringes at 10 μm and measure a mean contrast $V = 0.981 \pm 0.001$ with high repeatability over one week and high stability over a time-period of ~5 h. We show experimentally – as well as on the basis of modeling considerations – that the component has a single-mode behavior at this wavelength, which is essential to achieve high-accuracy interferometry. From previous studies, the propagation losses are estimated to be 0.5 dB/cm for this type of component. We also discuss possible issues that may impact the interferometric contrast.
Conclusions. The IO beam combiner performs well at the tested wavelength. We also anticipate the requirement of a closer matching between the numerical apertures of the component and the (de)coupling optics to optimize the total throughput. The next step foreseen is the achievement of wide-band interferograms.

Key words. instrumentation: high angular resolution – instrumentation: interferometers – methods: laboratory – techniques: interferometric

1. Introduction

Very recent results have demonstrated the potential of optical/IR interferometers to produce the first infrared astrophysical images of complex morphologies on the milli-arcsecond scale. These images have revealed unprecedented details about the highly distorted photosphere of the rapid rotator Altair (Monnier et al. 2007), they have produced the first direct view of the inner regions of a young circumstellar disk (Renard et al. 2010), and permitted us to measure the gas velocity map in the very close vicinity of a supergiant (Millour et al. 2011). These important breakthroughs would have not been possible without the help of imaging interferometers. The key to this technique is the astronomers' ability to simultaneously and coherently combine the beams from three or more telescopes. This permits the implementation of closure-phase techniques to obtain the interferometric visibilities amplitude and phase and allows the reconstruction of a complex astrophysical image. Although other techniques exist to retrieve the necessary phase information, increasing the number of sub-apertures and using Earth-rotation synthesis also drastically improves the UV plane coverage. This provides nearly snapshot reconstructed images, exhibiting high-fidelity and model-independent views of the object. However, the corollary of multi-beam combination is a significant increase in the optical complexity of the interferometer coupled to the need for high instrumental stability (mechanical and thermal) and a good level of control of the shape of the incoming wavefronts. In the past decade, instrumental research programs have demonstrated the feasibility of *single-mode* integrated optics (IO) components to enable both multi-aperture and high accuracy interferometric instruments using centimeter-scale devices (Malbet et al. 1999, and the following papers series). IO-based solutions have proven their astronomical potential with IOTA/IONIC (Berger et al. 2001; Monnier et al. 2004; Kraus et al. 2005) and VLTI/PIONER, putting them eventually at the heart of the future interferometric instrument GRAVITY at the VLTI. To date, this elegant solution and hence the resulting science has been limited to the near-infrared domain (J, H, K bands), yet there is an unquestionable astrophysical interest to extend this approach to the mid-infrared range, beyond

~3 μm. This is a key spectral range for the study for instance of objects with temperatures of ~100–600 K (e.g., the planet-forming regions around young solar-type stars, the location of the snow line Sasselov & Lecar 2000, and the debris disks morphologies as remnant of the planet formation process). Chemical bio-markers such as CO_2 or H_2O could be detected spectroscopically between 5 and 20 μm range to characterize the atmosphere of exoplanets in the habitable zone of solar-type stars (Cockell et al. 2009). In this respect, a space-based mid-infrared and multi-aperture *nuller* capable of producing a deep extinction of the stellar light (Angel & Woolf 1997; Mennesson & Mariotti 1997) would benefit as well from the compactness and stability of a IO beam-combiner. These different aspects have motivated a long-term investigation in the community to extend the IO instrumental solution beyond 2 μm (Mennesson et al. 1999; Laurent et al. 2002; Wehmeier et al. 2004; Labadie et al. 2006a, 2007; Hsiao et al. 2009). Because of the technological gap historically existing with the more mature near-infrared solutions, the mid-infrared extension has required a concerted R&D research effort between astronomers and photonics experts.

In this study, we demonstrate for the first time the fabrication and the operation of a two-telescope IO single-mode beam combiner for the mid-infrared spectral range around $\lambda = 10\,\mu$m. Chalcogenide glass materials are used for fabrication of this IO device, primarily because of the excellent infrared transparency in the 1–14 μm range and the photo-induced modification properties, i.e. the permanent or reversible increase in the glass refractive index induced by radiation (light, laser irradiation, etc.). The present work focuses primarily on the achievable interferometric contrasts and on the single-mode characterization of this new component.

2. Component design and manufacturing

2.1. Dimensioning and modal behavior

The opto-geometrical parameters of the Y-junction[1] are chosen to constrain the *single-mode* behavior in the 10 μm spectral range to benefit from the necessary spatial filtering of the combined wavefronts. Since a vast bibliography exists on the advantage of spatial filtering by single-mode waveguides for stellar interferometry and the corresponding theory (see Coude Du Foresto et al. 1997; Mennesson et al. 2002, and citing papers), we do not consider this here. In Fig. 1–left, we illustrate the geometry adopted in this study, which refers to an asymmetric-strip embedded waveguide-configuration. The electric field confinement in the y-direction is ensured by the high-index core layer of As_2Se_3 surrounded by a low-index substrate layer of As_2S_3, and air ($n = 1$). The confinement in the x-direction is ensured by an increase in the refractive index of the core layer over a well-defined region of the planar waveguide. The parameters considered to theoretically describe the modal behavior of the channel waveguide are the thickness $d = 3.8\,\mu$m and width $w = 6.5\,\mu$m of the strip, and a local increase in the refractive index $\Delta n = +0.05$. The refractive index values as a function of the wavelength for As_2Se_3 and As_2S_3 are taken from the literature (Savage 1965; Palik 1985; Klocek 1991; see examples in the caption of Fig. 1). We compute the theoretical bi-mode/single-mode cutoff wavelength – i.e. the wavelength above which only the fundamental mode is propagated – using the effective index approximation

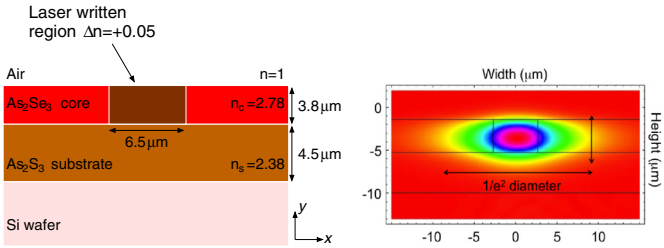

Fig. 1. *Left*: cross-section view of the Y-junction geometry. The high-index strip waveguide is bounded by As_2Se_3, As_2S_3 and air. Examples of refractive indices at 6, 8, 10, and 12 μm used in this study are n = 2.788, 2.783, 2.777, 2.774 for As_2Se_3 and n = 2.403, 2.394, 2.381, 2.364 for As_2S_3. *Right*: theoretical spatial distribution of the electric field for the $TE_{0,0}$ fundamental mode superimposed on the waveguide geometry. The vertical scale ranges from high (violet) to low (yellow) intensity.

approach, which is a classical numerical method in guided optics (Cheng & Lin 1990).

For comparison, the bi-mode/single-mode cutoff is computed for both the *planar* waveguide geometry and the *channel* waveguide geometry. The last value should also correspond to the cutoff wavelength for the Y-junction. With the parameters of Fig. 1–left, we obtain for the planar waveguide a cutoff value of 8.6 μm and 7.7 μm for the TE and TM polarization of the fundamental mode, respectively. We obtain for the channel waveguide a cutoff value of 8.7 μm (TE) and 7.6 μm (TM) for the fundamental mode, respectively. Beyond these cutoff wavelengths, the guiding structure is single-mode for each respective polarization, in particular at $\lambda = 10.6\,\mu$m, which is our operating interferometric wavelength in this work.

The fundamental mode $1/e^2$ diameter is ~18 μm and ~9 μm in the horizontal and vertical directions, respectively (see Fig. 1–right). This corresponds to large divergence half-angles (~40°) requiring fast coupling optics with numerical apertures of about $f/\# \sim 0.7$.

2.2. Fabrication of the Y-junction

The manufacture of the Y-junction device has benefitted from the PNNL[2] expertise on the design and fabrication of chalcogenide single-mode, low-loss waveguides for the thermal infrared, which nominally spans the range 8–14 μm. In two previous studies, Labadie et al. (2006b) and Vigreux-Bercovici et al. (2007) presented evidence of the ability of Arsenic–Sulfide-Selenium (As-S-Se) structures to produce an efficient confinement of infrared radiation at $\lambda = 10.6\,\mu$m. Hô et al. (2006) demonstrated the fabrication of single-mode *channel* waveguides using multi-layer deposition of arsenic-based thin films followed by laser writing (Efimov et al. 2001) to provide the lateral confinement of the field. The new step was then to fabricate and validate more complex guiding structures that are suitable to mid-infrared stellar interferometry.

A chalcogenide thin film structure was produced by means of the thermal deposition of a 3.8 μm core layer of As_2Se_3 on a 4.5 μm substrate layer of As_2S_3 according to deposition parameters described in Hô et al. (2006). The As_2Se_3 film is the high-index guiding structure with $n_{core} = 2.78$ at 10.6 μm, while As_2S_3 forms the substrate with $n_{sub} = 2.38$ at 10.6 μm. The lateral confinement was obtained using laser writing at $\lambda = 633$ nm and with writing power of 1 mW, which locally photomodified

[1] The Y-junction is a photonics device that can be used as either a beam-splitting device (1 input, 2 outputs) or a beam-combiner device (2 inputs, 1 input).

[2] PNNL: Pacific Northwest National Laboratory.

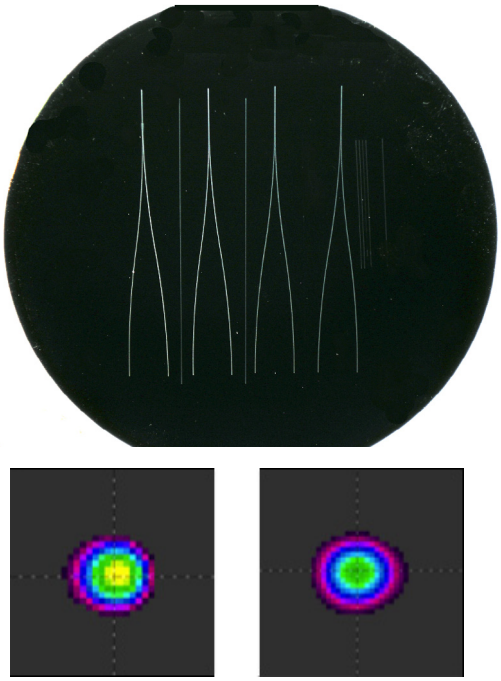

Fig. 2. *Top*: photo of the wafer containing the Y-junctions and the channel waveguides (see text for details). *Down*: qualitative snapshot views of the Y-junction outputs imaged at 8.5 μm to validate the beam-splitter configuration. The field mode is unresolved by the optical system.

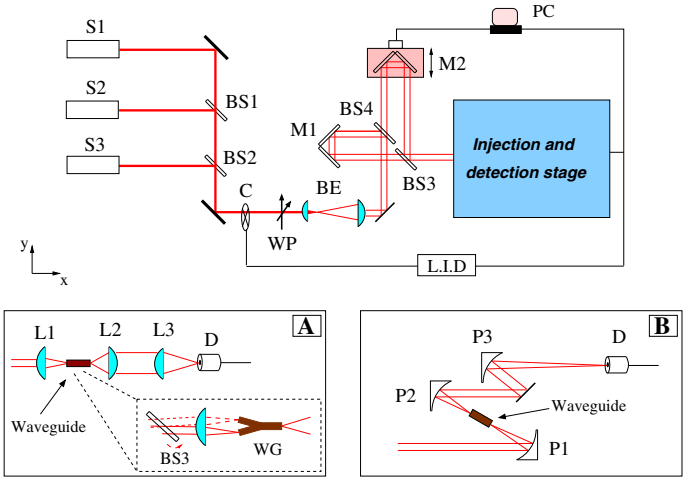

Fig. 3. Schematic view of the characterization testbench. *Top*: S_1 = black-body source; S_2, S_3 = laser sources; BS = beam-splitters; C = chopper; WP = quarter-wave plate; BE = beam expander. *Inset-A:* layout for the interferometric characterization; L = lenses; WG = waveguide; D = detector. *Inset-B*: layout for the spectroscopic characterization; P = off-axis parabolas.

the As_2Se_3 core layer, resulting in a higher refractive index. Previous results suggested that the photo-induced index difference achieved is $\Delta n \simeq 0.04$–0.05 under these processing conditions. To fabricate waveguides, the As_2Se_3 thin film substrate is translated about the focal plane of the focused writing laser beam using a computer-controlled translation stage moving at a speed of 4 mm/min. The waveguide width is slightly larger than the laser spot size of ~6 μm.

The length of the manufactured Y-junctions is ~50 mm long with a separation of 7 mm between the two arms. The top image of Fig. 2 shows the set of manufactured Y-junctions on the silicon wafer. This wafer also contains a set of straight waveguides written between the junctions that are used for testing and alignment purposes. The beam-splitting property of the Y-junction device was first tested by launching light into the single input. The bottom view of Fig. 2 shows the qualitative assessment of the beam-splitting capabilities of the device at 8.5 μm. The two Y-junction outputs were captured using an infrared microbolometer camera.

3. Experimental setup and procedure

Two different setups were used in this work. One is dedicated to the interferometric characterization of the devices at $\lambda = 10.6\,\mu$m, the second one focuses on the modal characterization of the components by Fourier transform spectroscopy in the 2–14 μm range. In Fig. 3, we present the general view of the setup, which we now briefly describe.

The interferometric unit: S_2 and S_3 are, respectively, the infrared CO_2 at $\lambda = 10.6\,\mu$m laser and the He-Ne alignment sources. The quarter-wave plate WP transforms the CO_2 flux polarization from a linear to a circular one. The beam-expander BE produces a collimated beam of almost 1-inch diameter, which then enters the interferometer. The infrared beam is divided by a system of beam-splitters, BS_3 and BS_4. The mirror-corner cube M_2 is mounted on a motorized translation stage and acts as the delay line to modulate the OPD. It can also be coupled to a piezoelectric motor for fine adjustment. In the monochromatic interferometric configuration, two options are available for waveguide coupling as depicted in the inset A of Fig. 3. One option is to recombine the two beams using BS_3 before injecting into the waveguide. The second option is to slightly tilt BS_3 to deviate the beam coming from M_2, which produces two distinct injection spots. These are used to feed the integrated optics junction, which plays the role of the beam combiner. In this configuration, we simply use refracting optics made of zinc selenide (ZnSe). To be as compliant as possible with the stringent numerical aperture of the current Y-junction inputs, we use an injection lens L_1 with $f/1.1$ clear numerical aperture. The Y-junction output flux is collected by the L_2+L_3 lenses system and focused on the MCT[3] detector D. The bench design makes it theoretically symmetric, assuming that (M_1, M_2) and (BS_3, BS_4) are "equal", with three reflections and one transmission per beam.

The spectroscopic unit: This was developed for broadband spectral characterization of *channel* waveguides as depicted in inset B of Fig. 3. Its configuration is very similar to the interferometric unit, but separately fed by the black-body source S_1 to cover the range from 2 μm to 14 μm. Hence, the light injection and collection optical system is based on off-axis parabolas (P_1, P_2, P_3) because of their achromatic nature. The broadband fringe pattern is produced by scanning the M_2 corner cube system.

The detection unit: The detection chain consists of the MCT detector itself, the beam chopper C to modulate the signal and a classical lock-in amplifier. The detected signal is digitally converted by the ADC card and recorded at a typical frequency of 10 Hz or faster. The experiment takes place in an open-air environment, with no active control of either the OPD or the beam

[3] MCT or mercury-cadmium-telluride.

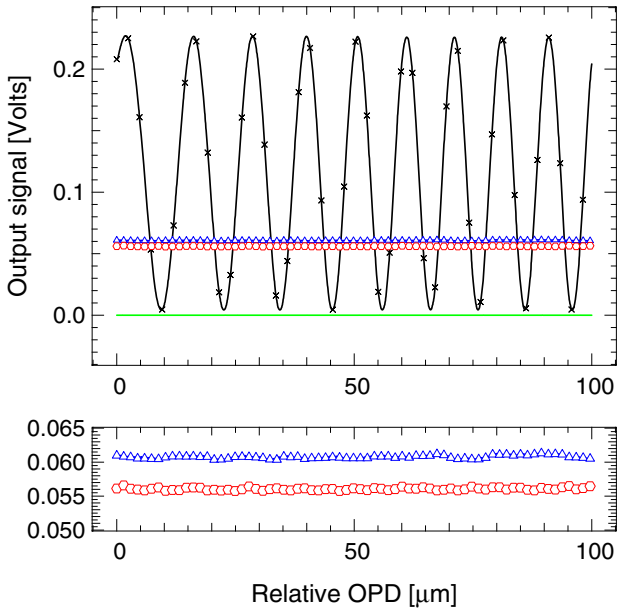

Fig. 4. *Top*: interferometric scan obtained with the Y-junction at 10.6 μm (black line+crosses); Photometry 1 (red curve with circles); Photometry 2 (blue curve with triangles); Bias signal (green solid line). *Bottom*: zoom on the photometric channels 1 and 2 in each arm of the Y-junction over the same OPD range as for the interferometric signal.

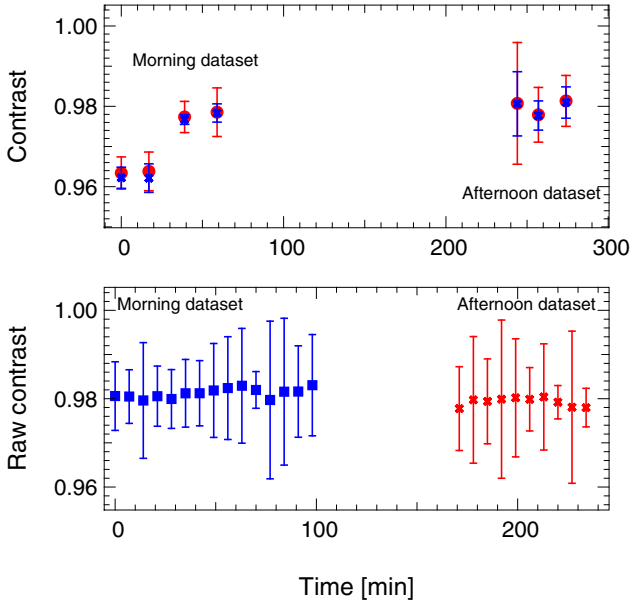

Fig. 5. *Top*: raw (blue crosses, V) and calibrated (red filled circles, $V_{\rm cor}$) visibilities measured from the dataset of October 14, 2010. *Bottom*: evolution as a function of time of the raw contrast obtained with the Y-junction on the dataset of October 6, 2010. The visibility points dispersion around the mean value is ±0.001.

jitter. Our measurements may potentially be sensitive to either the air turbulence or mechanical micro-vibrations in the room. In the future, we plan to develop a test-bench that allows the direct coupling of the individual beams in the component without passing the external beam-splitters BS_3 and BS_4, or to explore the viability of a fiber-link IO component (e.g. Berger et al. 1999; Haguenauer et al. 2000) exploiting the development of single-mode chalcogenide fibers (Ksendzov et al. 2007; Houizot et al. 2007). This aspect is particularly important to multi-beam combination.

4. Results and discussion

The Y-junction is the key element of an integrated-based mid-infrared interferometer. The important physical quantities to be characterized for our prototype at this stage are the achievable interferometric contrast and the single-mode operation range. Other interesting parameters to be studied in the future will be the total throughput, the aging effect of the component, and the impact of operation at cryogenic temperatures.

4.1. Temporally encoded fringes and monochromatic interferometric contrast

The Y-junction beam combiner has been characterized in the mid-infrared using the P_{22} line (10.611 μm) of a CO_2 laser. The setup described above permits us to inject flux into both channels, while the OPD is temporally modulated using the scanning delay line. The plots of Fig. 4 shows the monochromatic sinusoidal fringe pattern obtained by scanning eight periods. The photometric signal from each of the two channels is plotted around 0.05 V as a function of the OPD. The bias current of the detector is also plotted, although its very low level (~10 μV) has a negligible effect on the calibration. The fringe pattern displays a small chirp effect – i.e., a broadening of the period – from 0 to 100 μm, resulting from known small non-linearities of the translation stage. However, this has no great impact on the reliability of the measurement. The bottom plot of Fig. 4 shows a zoom on the photometry to illustrate the small photometric imbalance between the two input channels. In the following, the photometry imbalance is defined by $\rho = 1 - (I_1/I_2)$ with I_1 being the weakest flux, so $\rho = 0$ for a perfectly balanced system. In the case of Fig. 4, the plotted curves present an imbalance of $\rho \simeq 9\%$, which is then expected to have a negligible effect on the improvement of the interferometric contrast. We note that this is not true in the case of deep interferometric nulling, as demonstrated in Labadie et al. (2007). However, the work presented here does not focus on an optimized nulling measurement, but rather on the feasibility of an IO approach for mid-infrared interferometry.

In our specific case of a point-like source, the canonical expression for the monochromatic intensity interferogram is $I(x) = I_1(x) + I_2(x) + 2\sqrt{I_1(x)\,I_2(x)}\cos(\phi(x))$, where I, I_1, and I_2 are the interferometric, photometry 1, and photometry 2 signals, respectively. The quantity ϕ is the phase delay and x the OPD. The photometrically calibrated interferogram $I_{\rm cor}(x)$ is simply given by $I_{\rm cor}(x) = (I(x) - I_1(x) - I_2(x))\,/(2\sqrt{I_1(x)\,I_2(x)})$, where $I'(x) = 1 + I_{\rm cor}(x)$ is the normalized interferogram that would correspond to the observed signal if there were no photometric imbalance. The interferometric contrast can then be estimated in different ways, which essentially depends on the monochromatic or polychromatic conditions. We experimentally measure the raw and calibrated contrasts by calculating $V = (I_{\rm max} - I_{\rm min})/(I_{\rm max} + I_{\rm min})$ and $V_{\rm cor} = (I'_{\rm max} - I'_{\rm min})/(I'_{\rm max} + I'_{\rm min})$. The *min* and *max* indices correspond to the maximum and minimum values of the sine signal.

The plots of Fig. 5 illustrate the results of the interferometric calibration at two different dates, October 6 and October 14, 2010, respectively. The error bar associated with each visibility point is estimated by means of the propagation of experimental errors associated with the $I_{\rm max}$ and $I_{\rm min}$ quantities. In the top panel of Fig. 5, we compared the results for the raw visibilities V (blue crosses) to the photometry-calibrated visibilities $V_{\rm cor}$ (red

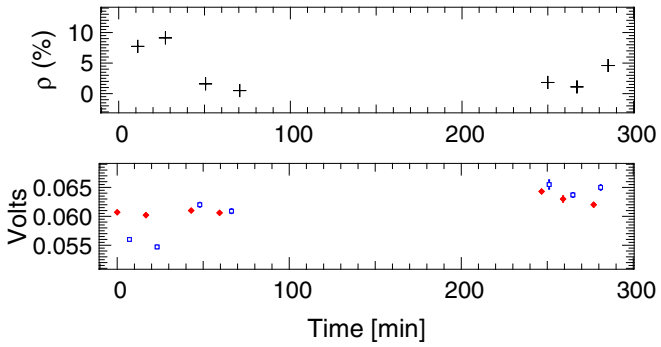

Fig. 6. *Top*: evolution as a function of time of the photometric imbalance between the two arms of the Y-junction. *Bottom*: evolution as a function of time of the mean and error in the photometry-1 (blue open squares) and photometry-2 (filled red diamonds) signals. In most cases, the error bar is equal to or smaller than the symbol itself.

filled circles) over several hours. Each interferometric scan was interleaved with successive acquisitions of the photometry channels I_1 and I_2 under the same conditions as the OPD scan. The individual interferometric visibilities span from 0.96 to 0.98. They appear to fluctuate slightly more in the first 50 min, then stabilize around 0.98. We note that the photometric calibration has little or no impact on the measured interferometric contrast, which is due to the small photometric imbalance of less than 10 % (see Fig. 6) or a theoretical degradation of 0.001 of the interferometric contrast. The bottom panel of Fig. 5 shows a better sampling of the temporal variations in the raw visibilities V on timescales of ~10 min. The interferometric contrast appears very stable to 0.1% over 5 h, with a time-averaged estimate of $V = 0.981 \pm 0.001$. Here, the error propagation method applied to each data does not appear to reflect the effective stability of the experimental visibilities, whose dispersion is smaller than the individual error bars.

Our experimental measurements clearly show that the Y-junction can successfully recombine interferometrically infrared beams and deliver high and stable contrasts. It is also interesting for future studies to anticipate other potential effects on the interferometric performance.

- A first consideration concerns the possible polarization mismatches that can diminish the interferometric visibility. The polarization states in the two channels are not monitored in this experiment. From Traub (1988), we know that a phase shift of 22.5° between the *s*-*p* differences of the two beams would be sufficient to introduce a visibility drop of $V = 0.02$ (*s* and *p* being the perpendicular and parallel components in the *xy* plane of incidence). Although this could be a considerable loss for future high contrast interferometric measurements, it remains quite acceptable for traditional V^2 interferometry. Such a small phase shift could be produced by either the bench optics (despite the apparent symmetry of the interferometer) or differential effects in the Y-junction arms. As an aside remark, we recall that the high dynamic range shown in Labadie et al. (2007) was obtained using a single-mode *and* single-polarization waveguide. Although not trivial, different practical solutions could be implemented on the bench to explore the polarization state of the combined beams before and after their coupling into the Y-junction.
- A second and more general consideration can be made about the single-mode behavior of the Y-junction. If we assume that the component is not "perfectly" single-mode – i.e. that the first higher-order mode is not completely filtered out because we are too close to the cutoff for instance – then we will experience residual phase errors (small misalignments, optical surfaces defects) that would not be compensated for with the photometric calibration (in other words, the waveguide does not perform perfectly well the flattening of the wavefront). Because the single-mode behavior at a given λ depends only on the component properties, its design must be carefully implemented to delimit the suitable single-mode range. Detailed analysis of the spatial distribution and propagation of the different modes in the structure as a function of the wavelength would certainly be helpful, although are not critical at this stage. The question of the modal behavior is addressed in the following section.

4.2. Spectroscopic characterization of the modal behavior

As explained in Sect. 1, the single-mode feature of the Y-junction is essential for an efficient spatial filtering of the incoming wavefront. To take advantage of the wavefront filtering capabilities of the component, it is therefore necessary to assess the spectral region where solely one mode is guided through the waveguide. By definition, the component has several cutoff wavelengths, which define different modal regimes (e.g. tri-mode, bi-mode, single-mode). These different regions can be identified by the *transmitted power method* (Lang et al. 1994), a technique routinely used to the characterize the single-mode fibers, and implemented as well in the field of astronomical instrumentation (Laurent et al. 2002). The principle of this method is based on the idea that the energy coupled into the waveguide at a given wavelength is distributed among the different propagation modes supported by the waveguide. As the wavelength varies from shorter to longer values, the number of supported modes decreases by one at each cutoff wavelength, and this can be traced in a transmission spectrum by identifying an abrupt dip in the guided flux intensity (Grille et al. 2009).

This technique was used here to characterize the modal behavior of the channel waveguides visible in Fig. 2 next to the Y-junction, which were manufactured following the same procedure. We verified the single-mode behavior of the component at 10 μm by performing Fourier transform spectroscopy between 2 and 14 μm with the setup described in Sect. 3. The bottom plot of Fig. 7 shows a zoom on the central white light fringe, which is acquired over a total OPD length of 2 mm resulting in a spectral resolution $\Delta\nu = 5\,\mathrm{cm}^{-1}$. We produced one reference spectrum of the black body source to be compared with the waveguide spectra, which are both presented in the top panels of Fig. 7.

The blue curve in the top panel is the raw emission spectrum of the black-body source acquired in the sensitivity range of the MCT detector. It includes the transmission by the lab atmosphere and the testbench components. Typical features can be observed such as the CO_2 absorption line around 4.2 μm or the water vapor absorption lines after 2.5 μm and between 5 μm and 7 μm. In the top-mid panel, the green and red curves are, under identical experimental conditions, two different measurements of the previous spectrum after coupling light into the chalcogenide channel waveguide. The black-body and waveguide spectra have been normalized to their peak intensity: indeed, because of the detection parameters (i.e. the gain of the lock-in amplifier) that changed between the two measurements, the two curves cannot be compared directly. Here the goal is limited to the identification of *relative* variations in the spectrum resulting from the waveguide characteristics.

The "waveguide" spectra include transmission effects related to the coupling input and output coupling efficiency, to

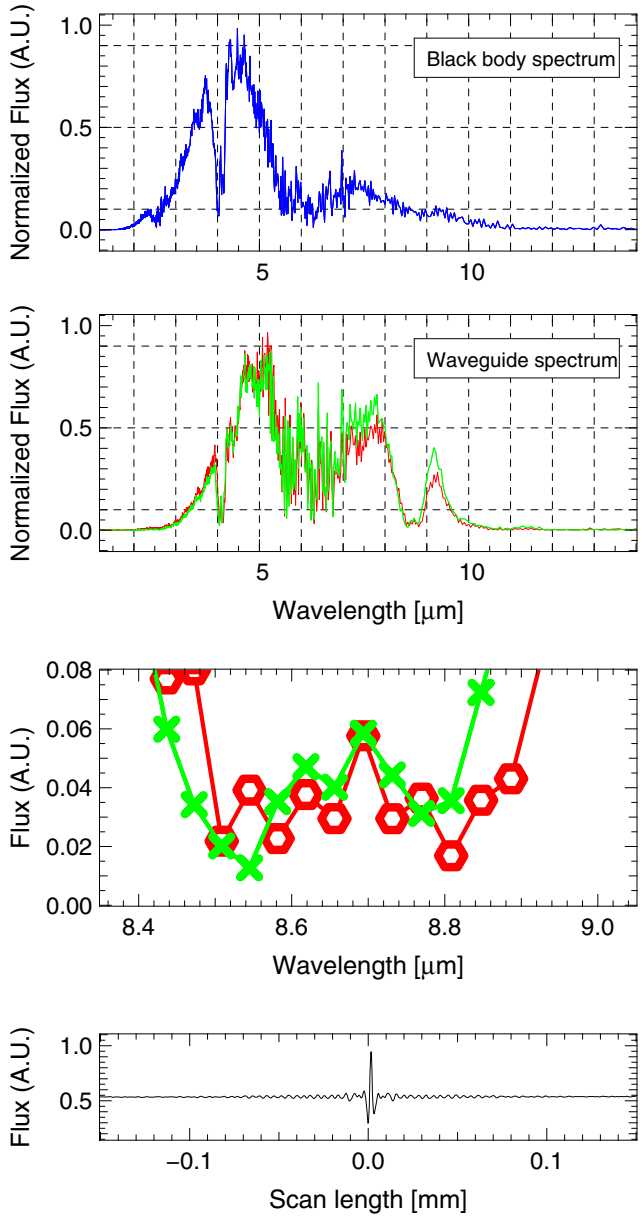

Fig. 7. *Top*: raw spectrum of the black-body source in the 2–14 μm range. Transmission spectra of the raw black body. *Central-top*: two measurements (red and green curves) of the black-body source spectrum after coupling into a chalcogenide channel waveguide with opto-geometrical parameters similar to the Y-junction ones. *Central-bottom*: zoom on the single-mode cutoff wavelength region. *Bottom*: zoom on the typical white light interferogram obtained with the FTS.

the transparency of the As_2Se_3 glass (i.e. propagation losses), and to the modal behavior of the waveguide, which is precisely the sought effect. Since the modal behavior change results from the loss of successive propagation modes from shorter to longer wavelengths, the amplitude of the transmission dip will be stronger as we go towards the lower-order cutoff wavelengths. Hence, we chose to focus here only on the search for the deepest bi-mode/single-mode transition since higher-order shallower jumps at shorter wavelengths would be more difficult to identify among the several features present in the spectrum. Therefore, the *transmitted power method* comes as a supporting technique to experimentally trace, in a restricted spectral range, the modal characteristics inferred theoretically, rather than a method for blind-searches of cutoff frequencies.

The waveguide plots of Fig. 7 reveal a clear intensity drop from ~8.0 μm down to ~8.5 μm in both measurements of the waveguide spectrum. A small double-dip feature is observable at ~8.5–8.6 μm and ~8.8 μm before the curve rises up. A large intrinsic absorption feature is very unlikely because of the homogeneous transparency of these chalcogenide glasses in this wavelength range (Savage 1965; Moynihan 1975). A possible interpretation may then be that we observe the bi-mode/single-mode transition of the waveguide with a measured cutoff around 8.5 μm. The rise-up of the curve after 8.8 μm corresponds to the well-known effect of energy transfer from first order to the fundamental mode following the cutoff. The double-dip feature observed at 8.6 μm and 8.8 μm in the waveguide spectrum may actually correspond to the close signatures of the planar and the channel waveguide, theoretically expected at 8.6 μm and 8.7 μm. Because the injection spot of the FTS setup is currently considerably larger than the channel waveguide cross-section (~30 μm vs. ~5 μm), a non-negligible fraction of the input energy is likely coupled to the surrounding planar waveguide, rather than solely to the channel waveguide, and collected back onto the detector. In this hypothesis, we find for the TE polarization a good agreement between the experimental and the theoretical values derived in Sect. 2.1, which are intrinsically very close. The 0.1 μm shift in the cutoff wavelength between theory and experience is within the range of uncertainty introduced by the manufacturing process to the index difference Δn and to the physical size of the waveguide, which ultimately define the modal behavior. If we were later able to reduce the spot size, keeping at the same time a good signal-to-noise ratio, this would certainly help to minimize this effect. For the TM polarization, the cutoff wavelength is expected by design to be at 7.7 μm, i.e. in a spectral region where we cannot achieve a high SNR because of the water absorption band. This suggests that the TM cutoff signature may be hidden in the quite noisy region of the spectrum. For the solid hypothesis of an observed cutoff wavelength and in spite of the small uncertainty highlighted above, this result confirms experimentally the single-mode behavior of the manufactured structure around $\lambda = 10\,\mu$m.

5. Conclusion

We have conducted a first laboratory study at 10 μm of the interferometric capabilities of a single-mode integrated-optics beam combiner in the context of instrumentation activities for multi-aperture IR interferometry. The Y-junction, manufactured by laser-writing, is composed of chalcogenide glasses, whose transparency is useful for integrated-optics beam combination in the L (3.2 μm), L' (3.8 μm), M (4.5 μm), and N (10 μm) bands.

We have demonstrated that there we can produce a high fringe contrast of 0.981 ± 0.001 at $\lambda = 10.6\,\mu$m, with high repeatability. This fringe contrast remains very stable over a significant time period of 5 h, even between two consecutive weeks. The component is also quite stable in terms of photometry variations (Fig. 6-bottom), which result from time-dependent laser drifts, mechanical instabilities of the motorized delay light impacting light coupling into the waveguides, or thermal instabilities of the laboratory environment. We have also verified and experimentally confirmed the single-mode range of the device beyond 8.5 μm.

In this study, we have also illustrated the importance of a proper numerical aperture optimization between the coupling optics and the waveguide structure. Large throughput losses

occur from both the numerical aperture mismatch and the Fresnel losses at each facet. The magnitude of these losses was not evaluated in this study. We are confident this can be solved by a well-coordinated design of the component and of the interface optics at the telescope. However, we already know from previous studies (Hô et al. 2006) that the intrinsic propagation losses of this type of device are as low as ~0.5 dB/cm. This is promising for the immediate future, where wide-band interferometric fringes constitute the next objective.

Although additional research in this area is required, this study can be seen as a first step towards the design, fabrication, and optimization of future instruments that exploit the benefits of astro-photonics (Bland-Hawthorn & Kern 2009) at mid-infrared wavelengths. Our study also demonstrated that we may be not so far from achieving an on-sky validation of this elegant approach for an operating interferometer. In the longer term, the development of a balloon-borne prototype interferometer at mid-infrared wavelengths comparable to what is already being achieved in the far-IR (Shibai et al. 2010) could probably benefit from these advances.

Acknowledgements. L.L. is funded by the Spanish MICINN under the Consolider-Ingenio 2010 Program grant CSD2006-00070: First Science with the GTC (www.iac.es/consolider-ingenio-gtc). This work was also supported by the US Department of Energy, Office of Nonproliferation Research and Development (NA-22). Pacific Northwest National Laboratory is operated for the U.S. Department of Energy by Battelle Memorial Institute under Contract No. DE-AC05-76RLO1830.

References

Angel, J. R. P., & Woolf, N. J. 1997, ApJ, 475, 373
Berger, J. P., Rousselet-Perraut, K., Kern, P., et al. 1999, A&AS, 139, 173
Berger, J. P., Haguenauer, P., Kern, P., et al. 2001, A&A, 376, L31
Bland-Hawthorn, J., & Kern, P. 2009, Opt. Express, 17, 1880
Cheng, Y., & Lin, W. 1990, Microwave Opt. Technol. Lett., 3, 419
Cockell, C. S., Léger, A., Fridlund, M., Herbst, T., & Kaltenegger, L. 2009, Astrobiology, 9, 1
Coude Du Foresto, V., Ridgway, S., & Mariotti, J.-M. 1997, A&AS, 121, 379
Grille, R., Martin, G., Labadie, L., et al. 2009, Opt. Express, 17, 12516
Haguenauer, P., Berger, J., Rousselet-Perraut, K., et al. 2000, Appl. Opt., 39, 2130
Hô, N., Phillips, M. C., Qiao, H., et al. 2006, Opt. Lett., 31, 1860
Houizot, P., Boussard-Plédel, C., Faber, A. J., et al. 2007, Opt. Express, 15, 12529
Hsiao, H., Winick, K. A., Monnier, J. D., & Berger, J. 2009, Opt. Express, 17, 18489
Klocek, P. 1991, Handbook of infrared optical materials, Optical Engineering (New York: Dekker), 428
Kraus, S., Schloerb, F. P., Traub, W. A., et al. 2005, AJ, 130, 246
Ksendzov, A., Lay, O., Martin, S., et al. 2007, Appl. Opt., 46, 7957
Labadie, L., Labeye, P., Kern, P., et al. 2006a, A&A, 450, 1265
Labadie, L., Vigreux-Bercovici, C., Pradel, A., et al. 2006b, Opt. Express, 14, 8459
Labadie, L., Le Coarer, E., Maurand, R., et al. 2007, A&A, 471, 355
Lang, T., Thevenaz, L., Ren, Z. B., & Robert, P. 1994, Meas. Sci. Technol., 5, 1124
Laurent, E., Rousselet-Perraut, K., Benech, P., et al. 2002, A&A, 390, 1171
Malbet, F., Kern, P., Schanen-Duport, I., et al. 1999, A&AS, 138, 135
Mennesson, B., & Mariotti, J. M. 1997, Icarus, 128, 202
Mennesson, B., Mariotti, J. M., Coudé du Foresto, V., et al. 1999, A&A, 346, 181
Mennesson, B., Ollivier, M., & Ruilier, C. 2002, Opt. Soc. Am. J. A, 19, 596
Millour, F., Meilland, A., Chesneau, O., et al. 2011, A&A, 526, A107
Monnier, J. D., Traub, W. A., Schloerb, F. P., et al. 2004, ApJ, 602, L57
Monnier, J. D., Zhao, M., Pedretti, E., et al. 2007, Science, 317, 342
Moynihan, C. 1975, J. Non Cryst. Solids, 17, 369
Palik, E. D. 1985, Handbook of optical constants of solids (New York: Academic Press Handbook Series), 623
Renard, S., Malbet, F., Benisty, M., Thiébaut, E., & Berger, J. 2010, A&A, 519, A26
Sasselov, D. D., & Lecar, M. 2000, ApJ, 528, 995
Savage, J. 1965, Infrared Phys., 5, 195
Shibai, H., Fukagawa, M., Kato, E., et al. 2010, in ASP Conf. Ser. 430, ed. V. Coudé Du Foresto, D. M. Gelino, & I. Ribas, 541
Traub, W. A. 1988, in European Southern Observatory Conference and Workshop Proceedings, ed. F. Merkle, 29, 1029
Vigreux-Bercovici, C., Bonhomme, E., Pradel, A., et al. 2007, Appl. Phys. Lett., 90, 011110
Wehmeier, U. J., Swain, M. R., Drouet D'Aubigny, C. Y., Golish, D. R., & Walker, C. K. 2004, in New Frontiers in Stellar Interferometry, Proc. SPIE, 5491, 1435